Progress in Quantum Electronics 50 (2016) 1–18

Contents lists available at ScienceDirect

Progress in Quantum Electronics

journal homepage: www.elsevier.com/locate/pquantelec

Quantitative imaging of cell membrane-associated effective mass density using Photonic Crystal Enhanced Microscopy (PCEM)

Yue Zhuo[a,d], Ji Sun Choi[b,e], Thibault Marin[f], Hojeong Yu[c], Brendan A. Harley[b,e], Brian T. Cunningham[a,c,d,*]

[a] Department of Bioengineering, University of Illinois at Urbana-Champaign, Urbana, IL 61801, USA
[b] Department of Chemical and Biomolecular Engineering, University of Illinois at Urbana-Champaign, Urbana, IL 61801, USA
[c] Department of Electrical and Computer Engineering, University of Illinois at Urbana-Champaign, Urbana, IL 61801, USA
[d] Micro and Nanotechnology Laboratory, University of Illinois at Urba na-Champaign, Urbana, IL 61801, USA
[e] Carl R. Woese Institute for Genomic Biology, University of Illinois at Urbana-Champaign, Urbana, IL 61801, USA
[f] 60 Hazelwood Dr, Champaign, IL 61820, USA

ARTICLE INFO

Keywords:
Photonic Crystal Enhanced Microscopy (PCEM)
Photonic Crystal (PC)
Photonic Crystal Slab
Photonic Crystal Biosensor
Live Cell Imaging
Label-free Imaging
Stem Cell
Cancer Cell
Refractive Index (RI)
Peak Wavelength Value (PWV)
Peak Wavelength Shift (PWS)
Mass Density (MD)
Cell Membrane-associated Effective Mass Density

ABSTRACT

Adhesion is a critical cellular process that contributes to migration, apoptosis, differentiation, and division. It is followed by the redistribution of cellular materials at the cell membrane or at the cell-surface interface for cells interacting with surfaces, such as basement membranes. Dynamic and quantitative tracking of changes in cell adhesion mass redistribution is challenging because cells are rapidly moving, inhomogeneous, and nonequilibrium objects, whose physical and mechanical properties are difficult to measure or predict. Here, we report a novel biosensor based microscopy approach termed Photonic Crystal Enhanced Microscopy (PCEM) that enables the movement of cellular materials at the plasma membrane of individual live cells to be dynamically monitored and quantitatively imaged. PCEM utilizes a photonic crystal biosensor surface, which can be coated with arbitrary extracellular matrix materials to facilitate cellular interactions, within a modified brightfield microscope with a low intensity non-coherent light source. Benefiting from the high sensitivity, narrow resonance peak, and tight spatial confinement of the evanescent field atop the photonic crystal biosensor, PCEM enables label-free live cell imaging with high sensitivity and high lateral and axial spatial-resolution, thereby allowing dynamic adhesion phenotyping of single cells without the use of fluorescent tags or stains. We apply PCEM to investigate adhesion and the early stage migration of different types of stem cells and cancer cells. By applying image processing algorithms to analyze the complex spatiotemporal information generated by PCEM, we offer insight into how the plasma membrane of anchorage dependent cells is dynamically organized during cell adhesion. The imaging and analysis results presented here provide a new tool for biologists to gain a deeper understanding of the fundamental mechanisms involved with cell adhesion and concurrent or subsequent migration events.

1. Introduction

Cell adhesion, the means by which cells communicate with neighboring cells and the surrounding matrix *in vivo*, is critical for

* Corresponding author at: Department of Electrical and Computer Engineering, Department of Bioengineering, University of Illinois at Urbana-Champaign, Urbana, IL 61801, USA.
E-mail address: bcunning@illinois.edu (B.T. Cunningham).

http://dx.doi.org/10.1016/j.pquantelec.2016.10.001

Available online 04 November 2016

maintaining normal cell functions during homeostasis [1,2]. Cell adhesion not only provides structural support, but also contributes to functional processes crucial for proliferation and survival [3,4]. Recently, the importance of adhesion phenotyping of single cells has been highlighted as growing evidence suggests that changes in cell adhesion profiles may be correlated with changes in cellular states [5], fate decisions [6], and disease progression/prognosis [3,7]. For these purposes, it is highly desirable to collect cell adhesion-related information of single cells to delineate the role of adhesion and to elucidate the associated biological mechanisms.

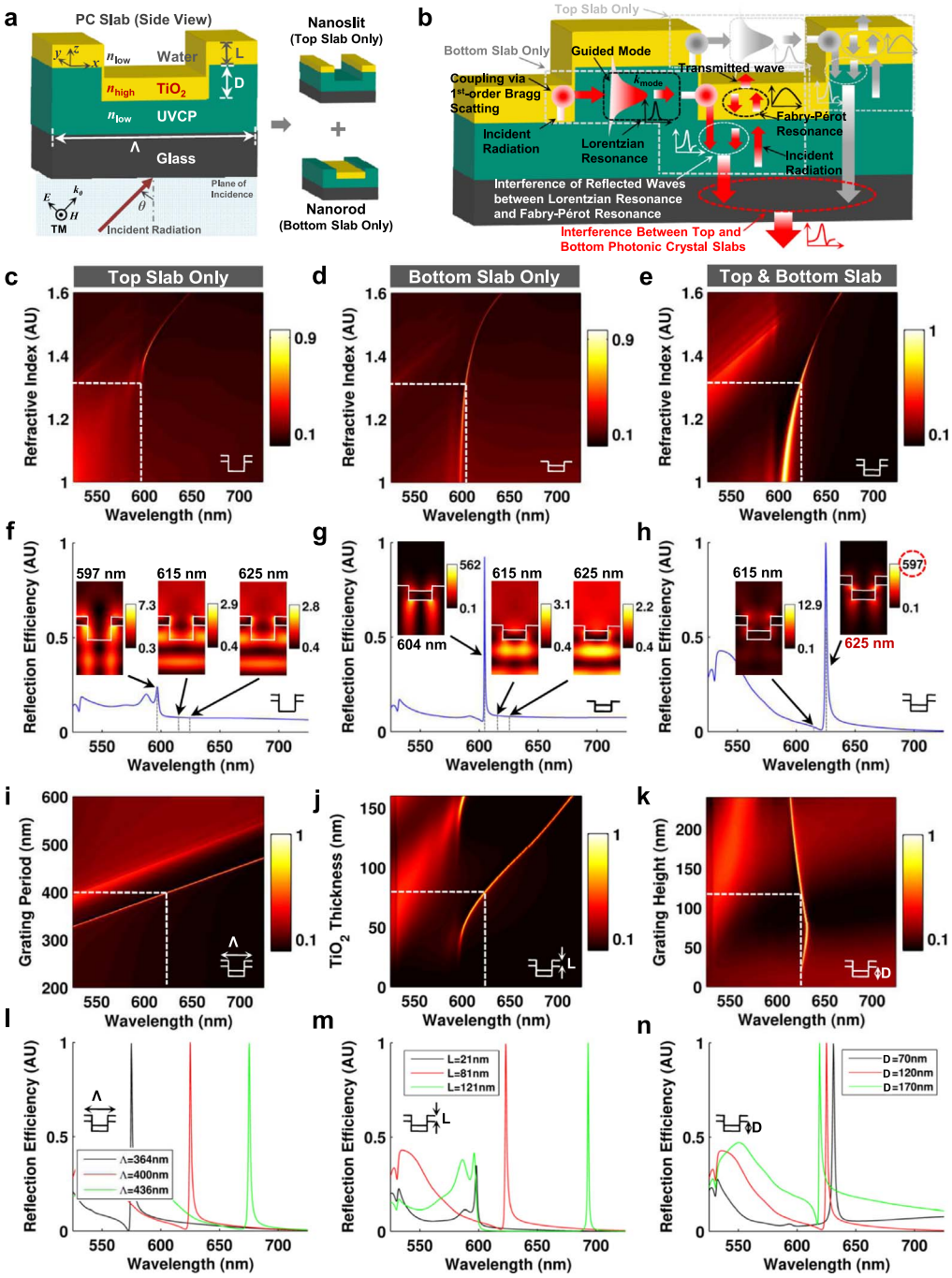

Fig. 1. *Principles and Properties of Photonic Crystal (PC) Slab Biosensor.* (a) Schematic of the PC surface and its dimension parameters. (b) Schematic drawing of the resonant mode in the PC biosensor. The 2D graphs of reflection efficiency according to the change of the background refractive index for (c) Nanoslits-only on the top of the grating, (d) Nanorods-only on the bottom of the grating, and (e) Nanoslits and Nanorods (both PC slabs). (f–h) plot the 1D reflection spectra for the above three nano-structures. Insets: (near-field) normalized electric field intensity distributions ($|E/E_0|^2$) within a grating period at different wavelengths (on/off resonance). The 2D graphs (i-k) and 1D spectra (ι-n) of reflection efficiency correspond to the geometry variations of the PC slab biosensor: (i,l) grating period Λ, (j,m) thickness of the TiO_2 coating L, (k,n) grating height D.

However, technical limitations of existing cell microscopy approaches and the complexity of cell adhesion processes have been a major hurdle for decades. During cell adhesion and subsequent motile events, dynamic redistribution of cellular materials occurs particularly along the cell membrane, which corresponds to the cell-surface interface in the case of an *in vitro* setting where cell adhesion is typically studied on top of a biofunctionalized two dimensional (2D) surface. Cell plasma membranes, including the associated active soft matter within the membranes, exist within non-equilibrium states with unusual physical and mechanical properties that are difficult to measure or predict with traditional imaging methods. For instance, high axial resolution is required when studying cell-surface interaction because it is essential to eliminate the background scatter disturbance from above and beneath the imaging plane. Nevertheless, several technologies based on a diverse set of imaging principles, including far-field and near-field imaging modalities, have emerged to address these difficulties [8–19]. For example, in far-field imaging, confocal fluorescence microscopy is used to probe changes in the cell membrane by using a diffraction limited focal volume of laser excitation, providing an axial resolution of 800~900 nm. However, confocal fluorescence microscopy suffers from background excitation below or above the focal plane, in addition to the challenges presented by slow scanning speeds and fluorophore photobleaching [12]. White-light diffraction tomography (WDT) [18] has emerged recently as a promising label-free method based on the principle of phase imaging that is capable of measuring three dimensional (3D) structures of the cell body, which has demonstrated ~900 nm axial resolution.

Another approach that offers high axial resolution is near-field microscopy (axial resolution is typically smaller than 200 nm, which is beyond the diffraction limit in spectra range of visible light (400~700 nm) in the axial direction), including Total Internal Reflection Fluorescence (TIRF) microscopy, and Surface Plasmon Resonance Microscopy (SPRM). TIRF microscopy has been widely applied to the study of cell substrate interactions with fluorescent tags using a specialized objective lens that creates a spatially restricted resonant electromagnetic field (called evanescent field) on top of a substrate surface when total internal reflection occurs [8,10,13]. The axial resolution of TIRF microscopy is typically 100~200 nm, resulting from high intensity illumination from the evanescent field. Like all fluorescence-based cell imaging approaches, photobleaching precludes long term study of cell behavior by TIRF microscopy. SPRM is a label-free imaging modality which utilizes the surface plasmon resonance of metallic surfaces (e.g. typically a thin gold layer) to measure the refractive index (RI) change on the metal surface [9,14]. In surface sensing, SPRM can achieve several tenths of nanometer in axial spatial resolution with surface electromagnetic waves coupled to oscillating free electrons of a metallic surface that propagate along the surface. However, the lateral propagation in SPRM is not restricted on the flat metal surface which leads to limited lateral spatial resolution (e.g. typically micrometer scale). To address the above challenges, we employ Photonic Crystal Enhanced Microscopy (PCEM), a novel label-free microscopy approach with near-field imaging on nano structured dielectric surfaces and associated advanced data analysis, to study cell-surface interactions. PCEM offers a platform for quantitative and dynamic imaging of cell adhesion by measuring changes occurring only at the cell-surface interface (< 200 nm) arising from cellular effective mass density redistribution associated changes with adhesion events.

PCEM utilizes the cell membrane and its associated protein components as an integral part of the photonic crystal (PC) structure. The PC surface is a subwavelength nano structured material with a periodic modulation of refractive index that acts as a narrow bandwidth resonant optical reflector at one specific wavelength and incident angle [20–44]. The high reflection efficiency of the PC at the resonant wavelength/angle combination is the result of the formation of electromagnetic standing waves on its surface that extend into the surrounding medium in the form of an evanescent electromagnetic field. In a traditional one dimensional (1D) *PC stack* (e.g. a multilayer stack of materials with alternating dielectric constants, often referred to as Bragg mirrors) [25,31,45], the periodicity is normal to the substrate plane and a photonic band gap is formed for light with the evanescent part of the wave vector normal to the surface. When used in biosensing or bioimaging, this PC structure utilizes the surface electromagnetic waves bound to the multilayer (named Bloch surface waves) to measure the dielectric changes at the substrate surface. However, this type of PC structure has not been used for realizing high spatial resolution biosensor imaging since its Bloch surface modes are not confined laterally (rather they propagate along the plane of the substrate surface). Another type of important PC structure is the *PC slab*, which consists of a periodicity of RI contrast (e.g., 1D or 2D) in the plane of the substrate surface introduced by alternating a high-RI guiding layer with low-RI materials. A PC slab not only supports in-plane guided modes that are confined by the slab completely (which cannot couple to external radiation), but also supports guided-mode resonances (referred to as quasi guided modes or leaky modes) which can couple to the external environment. Therefore, the maximum intensity of the electromagnetic field can be observed both in the high-RI layer and in the evanescent part outside of the PC slab.

As shown in Fig. 1a, the PC biosensor used in this work can be viewed as a quasi-3D nanostructure (see Methods Section 4.1.2 for details), which can be decomposed into two 1D PC slabs (Nanoslits with high-RI materials only on the top of the grating, and Nanorods with high-RI materials only on the bottom of the grating) interfering with each other in a complex manner. Each 1D PC slab is composed of a low refractive index (RI) grating structure (e.g., UV curable polymer, n_{UVCP}=~1.5), a high RI coating (e.g., TiO_2, n_{TiO2}=~2.4), and a thin layer of cellular material (including the cell plasma membrane and a thin layer of intracellular material near the membrane, n_{cell}≈1.35~1.38) on a glass (n_{glass}=~1.5) substrate. When broadband collimated light illuminates this quasi-3D PC slab from below, there are three types of coupling taking place simultaneously between the incident light and the PC structure (Fig. 1b). First, the incident light couples to the discrete in-plane guided mode supported by the PC slab via first-order forward and backward Bragg scattering when satisfying the momentum-matching condition (as described in Eq. (3)), and creates a narrow resonance peak in the spectra with Lorentzian lineshape (referred to as resonant Wood's anomalies). Second, the incident light couples to the continuum broadband vertical Fabry–Pérot (F–P) nanocavity and the resonance peak shifts with a broadband peak in spectra. The above two processes interfere with each other and lead to an interfered reflectivity spectrum for each layer of PC slab, which can be described as a phenomenological Fano interference model. Third, the two reflectivities from nanoslits (Top-slab-only, as in Fig. 1c and f) and nanorods (Bottom-slab-only, as in Fig. 1d and g) interfere with each other and yield the total reflectivity

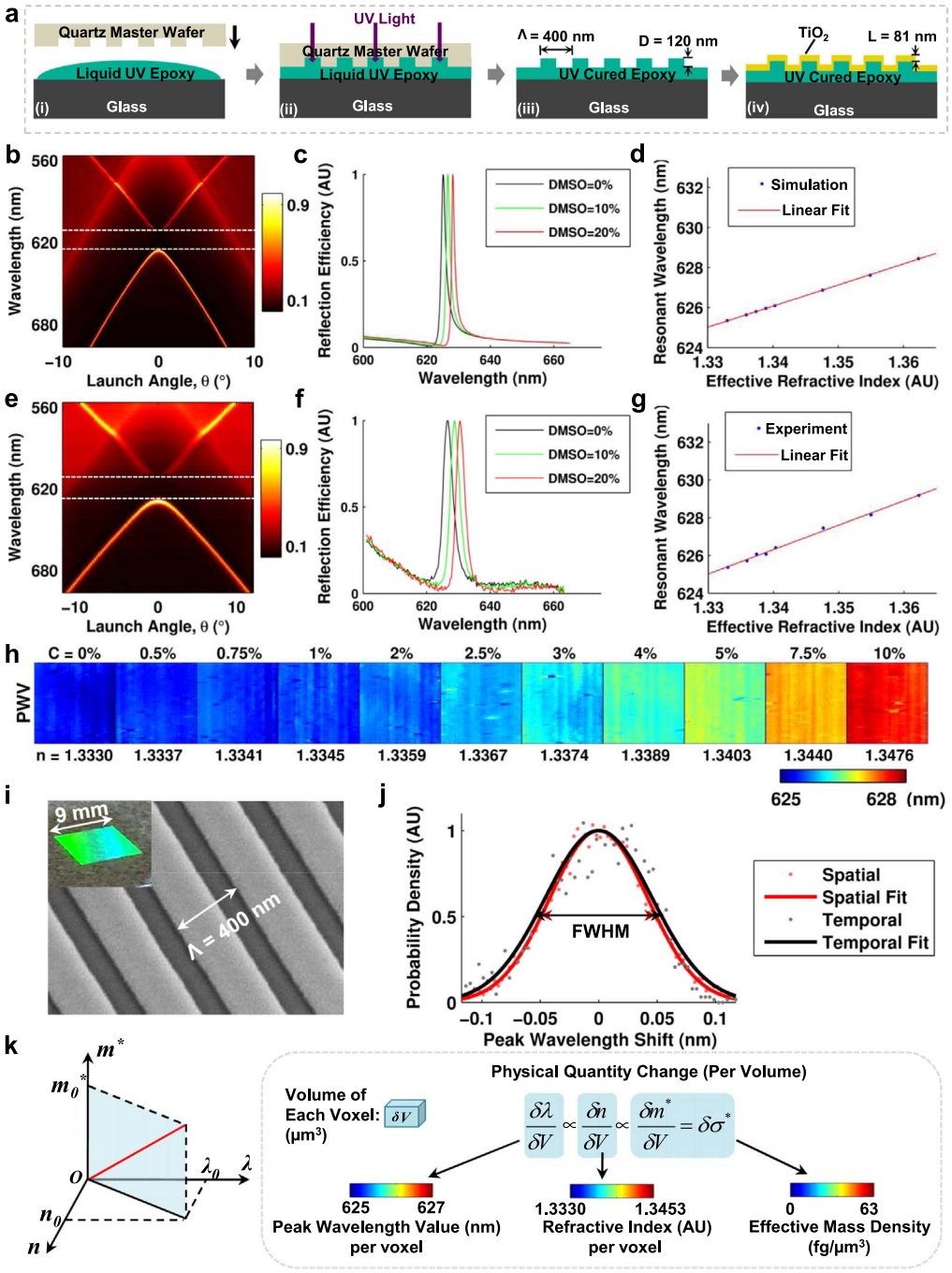

Fig. 2. *Fabrication and Characterization of PC Slab Biosensor*. (a) Fabrication process of the PC slab surface based on nanoreplica molding (i–iii) and a single-layer coating (iv). Dispersion maps of the PC slab biosensor used in PCEM for (b) Simulation and (e) Experimental Results. Normalized reflection efficiency for (c) Simulation and (f) Experimental Results. Sensitivity curve linearly fitted from the (d) Simulation and (g) Experimental Results. (h) PWV images of DMSO solution with different concentrations (representing different effective refractive indices). (i) SEM images of the PC slab surface with grating period of 400 nm. Inset: photo of a fabricated PC slab biosensor with area of 9×9 mm^2. (j) Spatial (in red) and temporal (in black) optical-path-length noise levels of the background region (the dotted lines represent raw data, and the solid lines indicate Gaussian-fits). (k) Schematic of the physical quantity conversion from measured shift of peak wavelength value (PWV) to the change of cellular effective mass density (MD) in each voxel.

as a Fano interference resonance (Top and Bottom slab, as in Fig. 1e and h). Although the resonance mode is complex compared with the traditional 1D or 2D PC slabs, one of the obvious advantages of this quasi-3D PC nano slab structure is easy fabrication (e.g. nanoreplica molding for the nano grating structure, and a single thin-layer coating for the high-RI material), thus preserving highly stable and predictable optical properties [39–41]. Simple fabrication offers benefits for single-use disposable detection in high-throughput screening medical diagnostic and label-free biosensor/microscopy applications.

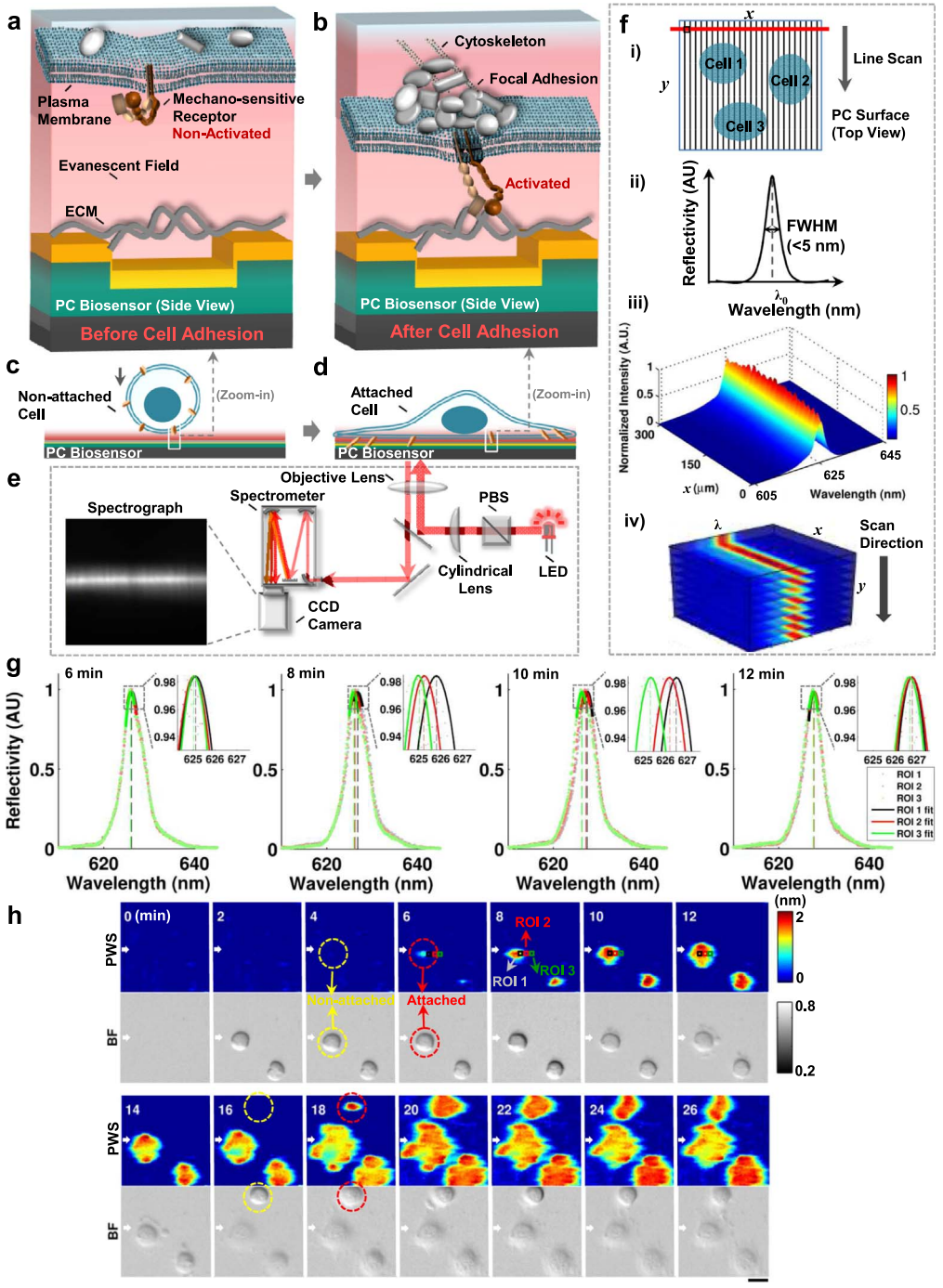

Fig. 3. *Principle of Cell Adhesion on a PC Slab Biosensor in PCEM*. (a,c) Before cell adhesion: ECM molecules are immobilized on the PC slab biosensor surface. (b,d) After cell adhesion: Transmembrane mechano-sensitive receptors are activated after adhesion, and focal adhesions are formed on the plasma membrane to form a link between receptors and the cytoskeleton. The effective refractive index is locally increased in each voxel on the PC slab surface. (a,b) for the zoomed-in view of individual mechano-sensitive receptor molecules and (c,d) for the view of whole cells. (e) Schematic of the PCEM system. (f) Data acquisition of PCEM: i) represents the line-scan in y direction on PC slab surface; ii) represents the reflectivity spectrum at each voxel; iii) represents the acquired 2D spectra graph for each line on the PC slab surface; iv) represents the resulting 3D spectra data acquired after each line-scan. (g) Representative peak wavelength shift (PWS) in Spectra for different locations within or near one stem cell (mHAT9a) on the PC slab surface (marked with black, red and green rectangles on the PWS images in (h) from 6~12 min, respectively). (h) Label-free and dynamic detection of stem cell adhesion using PCEM. 1 & 3 rows: PWS images (unit: nm); 2 & 4 rows: brightfield (BF) images (unit: AU). Stem cells (mHAT9a) were seeded on a fibronectin-coated PC slab biosensor surface and started to attach in ~5 min (higher intensity in PWS images indicates a higher localization of cellular material at the PC slab surface, which can be expected during cell spreading). Bar length=10 μm.

Simulations performed using the Finite Difference Time Domain (FDTD) method show the spatial distribution of the evanescent field (Fig. 1f–h Insets), which extends, on average, ~62 nm into the aqueous medium on top of the PC slab (maximum thickness ~200 nm, as shown in S-Fig. 1). By extracting the peak wavelength value (PWV) which is determined by the local dielectric permittivity of the cellular material (with a fixed dimension of PC), a PWV image can be used to effectively detect and quantify cell attachment to the PC surface. Changes in the optical density of a cell during adhesion will lead to a modified resonance condition and cause a peak wavelength shift (PWS) in the measured local reflection spectrum. As mentioned earlier, the photonic band gap (simulated as in Fig. 2b and measured as in Fig. 2e) strictly limits lateral propagation of light on the PC surface. Therefore, the PC exhibits strong optical confinement of incident light into an infinitesimal volume that interacts selectively with surface adsorbed cell components, while being completely insensitive to the components of the cell body that are not engaged with the surface. The PC surface can thus act as a proxy for a biological surface with the capacity to detect changes in the amount of cellular materials accumulating on top (within the evanescent field), which presents a platform ideal for adhesion phenotyping of live cells.

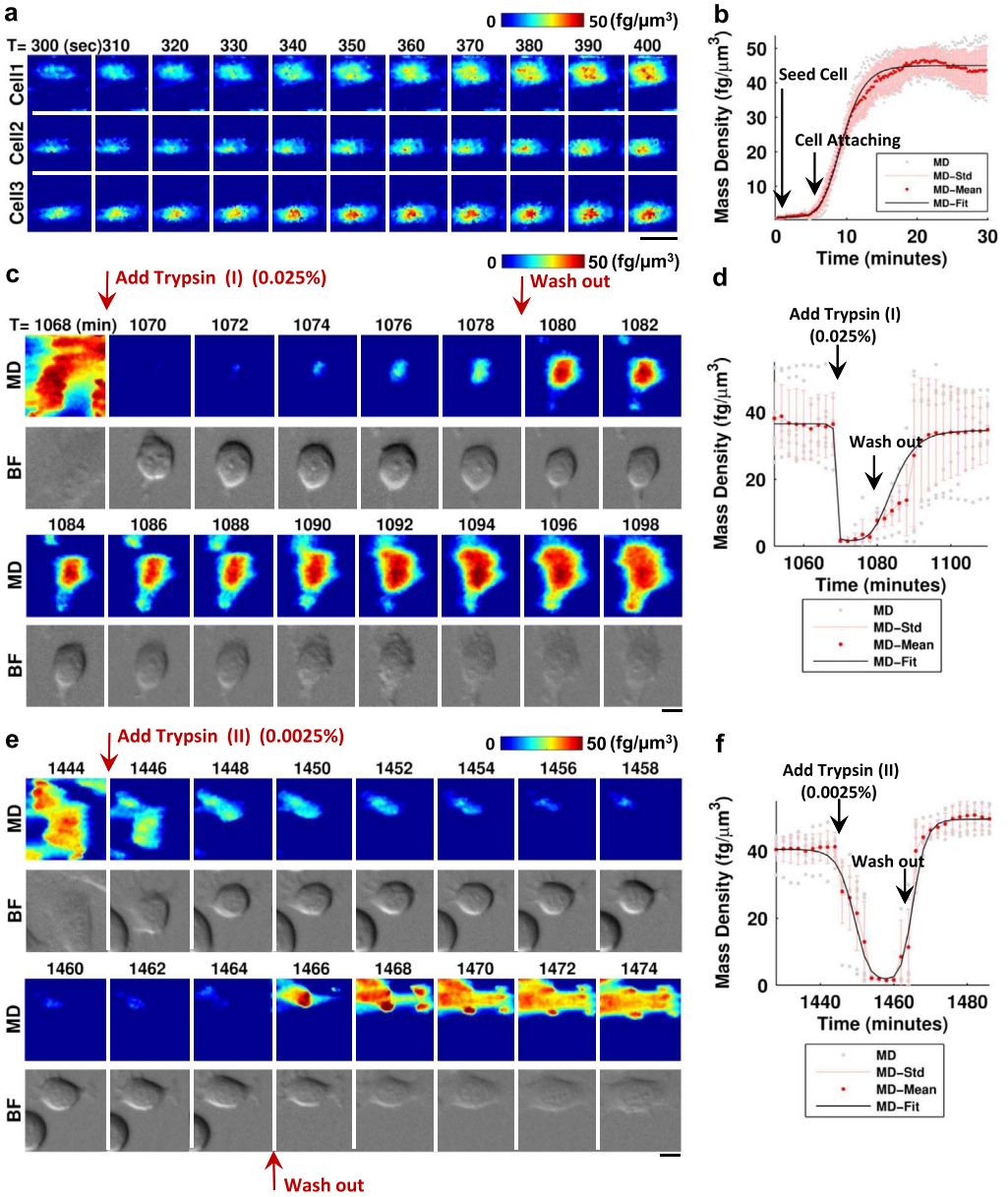

Fig. 4. *Short Term and Long Term PCEM Imaging and Corresponding Kinetics for Stem Cell Adhesion and Drug-responses.* (a) Short term imaging (0~30 min) of membrane-associated effective mass density images for initial cell (mHAT) adhesion at time interval of 10 s/frame (unit: fg/μm^3). (b) Cellular membrane-associated effective mass density (MD) response at initial adhesion (N=6 cells). Long term imaging (0~25 h) of membrane-associated effective mass density images for drug-responses with cell (mHAT) attachment, detachment, and reattachment: addition of (c) high and (e) low concentration of Trypsin to detach cells, incubate, wash out drug, and then change to fresh media (time interval of 2 min/frame) (unit: fg/μm^3). Cellular effective mass density responses are modulated by (d) high and (f) low concentrations of Trypsin and different incubation times (N=7 cells). Bar length=10 μm.

2. Results and discussion

2.1. Verifying measurement in PCEM imaging

While PCEM directly measures localized shifts in the resonant wavelength on the PC surface, it is helpful to consider what the PWS information physically represents in the context of cell attachment. When a cell comes into contact with the PC evanescent field, its lipid bilayer and cell-associated protein structures displace the aqueous cell growth media (Fig. 3a–d), effectively replacing a lower-RI material (n_{water}=~1.333) with a higher-RI material (n_{cell}≈1.35~1.38). In such a small dynamic range, PWS is approximately linearly proportional to the change of the effective RI of the resonant mode, which resides in the cell, the TiO_2 thin film, and the polymer grating material underneath the TiO_2. Fig. 2c, d, f and g demonstrate the linear relationship between the PWS and change of effective RI estimated via simulation (Fig. 2c and d) and verified experimentally (Fig. 2f and g) as modulating the RI by covering the PC surface with solutions of different concentrations of dimethylsulfoxide (DMSO) in water (PWV images are shown in Fig. 2h). Therefore, PWS can be converted to an effective RI shift for a PC biosensor with a known refractive index sensitivity (measured as ~160 nm/RIU (Refractive Index Unit) in this work). In the context of cell attachment label-free imaging, changes in effective RI represent the dielectric permittivity of the attached cellular material, which is distinct from the physical mass density of the material. Although some cell membrane associated components (such as the lipid bilayer or actin filaments) have specific physical orientations with respect to the resonant electromagnetic field vector (which is in the z-axis perpendicular to the PC surface), for simplicity, here we will make the approximation that the dielectric permittivity of the lipid and protein components of attached cells are lossless and homogeneous in all directions within each molecule. Characterization of the dielectric properties of live cell materials has shown that a change in the local membrane-associated effective mass density (MD) can be viewed approximately linearly proportional to a change of RI (see Methods Section 4.3.2 for details) [46–48]. Measurements indicate that there are only ~5% variations across a wide range of typical biological molecules for this linear relationship [46,47]. Based on this relationship, the PWS images obtained by PCEM can be used to represent the effective mass (referred to as dry mass) density of the cell membrane and its associated proteins within the evanescent field region (Fig. 2k).

With this approach of directly relating PC biosensor resonant wavelength shifts to cell membrane-associated effective mass density shifts, we may consider the total effective mass change that occurs within any individual voxel or within a region of interest (ROI). For example, a series of background images with water only (without cells) on the PC surface were acquired with a ROI of ~85×45 μm^2 for ~7 h. The resulting spatial and temporal histograms (with Gaussian fitting curves) can be used to quantify the imaging resolution for observing resonant wavelength shifts for PCEM (Fig. 2j). More specifically, the full width half maximum (FWHM) of the temporal histogram is ~0.064 nm, which is calculated based on the measured PWV in the ROI for a user-selected period of time (i.e. 7 h). The FWHM of the spatial histogram is ~0.059 nm, which is calculated based on the measured PWV within a user-selected area of the PC surface (i.e. ~85×45 μm^2). Using PCEM, we are thus able to observe PWS above the background noise as small as ~0.06 nm (spatiotemporal), correlating with the ability to observe changes in cell membrane-associated effective mass density as small as 1.9 fg/μm^3 (equivalent to a effective mass of ~0.04 fg within an individual voxel with a volume of δV=~0.6^2×0.06 μm^3). When a single cell is attaching to the PC surface, the measured PWS within a voxel can be as high as ~2 nm, which corresponds to a effective mass density change of ~63.2 fg/μm^3 (effective mass change of ~1.4 fg in a voxel). Importantly, cell membrane-associated effective mass density images may be obtained over time scales of interest for understanding many aspects of cell behavior. The shortest time interval demonstrated thus far between subsequent PCEM images is 10 s (Fig. 4a–b, S-Fig. 2), enabling the potential for observation of dynamic membrane protein transportation or focal adhesion (FA) assembly/disassembly. As the PCEM is integrated with a cell incubator environment, processes may also be observed over time periods that extend for several hours (Fig. 3h). Furthermore, because the imaging approach is label-free, the same cells may be revisited on subsequent days (Fig. 4c–f, S-Fig. 3) to observe very long-term behavior such as stem cell differentiation.

2.2. Quantitatively measuring live-cell membrane-associated effective mass density (MD)

Valuable surface attached cellular information can be extracted directly from the PCEM images through observation of local variations in PWS (Fig. 3g–h and S-Figs. 2–3). As shown in Fig. 3g–h, the sequence of reflectivity spectra and corresponding PWS maps (at different time) indicates the movement of an ultra-thin layer of cellular material that gradually contacts the PC surface. Compared with ordinary brightfield images in which cell attachment cannot be easily observed, there are several unique properties within PCEM images that we illustrate in Fig. 3h using dental epithelial stem cells (mHAT9a) attached to a fibronectin coated PC surface (at 37 °C and humidified 5% CO_2 chamber environment). First, at the initial stage of cell introduction (Fig. 3h, within ~5 min), even if a cell is physically present within the field of view, it may be present on the surface but not engaged with the substrate underneath. This pre-attachment phase precedes subsequent attachment that involves transmembrane mechanosensitive receptors (e.g. integrins) that actively bind the extracellular matrix (ECM) protein coating (e.g. fibronectin) immobilized on the PC surface, which appear as a PWS. This phenomenon can also be observed from the difference between the PWS images and the brightfield images in a late-attached cell (top cell) in Fig. 3h (at ~16 min). Brightfield images indicate that all nearby cells physically present on the PC biosensor surface, but it can be clearly observed from the PWS images that the middle and bottom cells are truly attached while the top cell is not. Second, compared to the initial cell area presented by the cell body shown in the brightfield image, the PWS image indicates that the actual contact area between the cell and the surface underneath is much *smaller* than the cell diameter (Fig. 3h, at ~6 min). Thus, PWS images may influence the current understanding of how cells land upon and subsequently interact with the substrate surface, and correspondingly how the cellular force is initially distributed and redistributed. Third, in

contrast to the static cell area depicted in the early attachment period (during 4~8 min) as shown in the brightfield images in Fig. 3h, PWS images indicate that the attached cell area *dynamically extends* from the center to a larger area with an estimated average boundary velocity of ~0.1 μm/min. This initial velocity corresponds with the reported polymerization speed of cytoskeleton molecules (e.g., microtubule is 0.8~1 μm/min) *in vitro* [49]. Finally, the PWS images demonstrate a highly non-uniform and dynamic cellular material distribution during adhesion processes (Fig. 3h, 16~26 min), with features that may correspond to different cell motion modalities, cellular force redistribution, and cell-substrate interactions. Such rich information of cellular

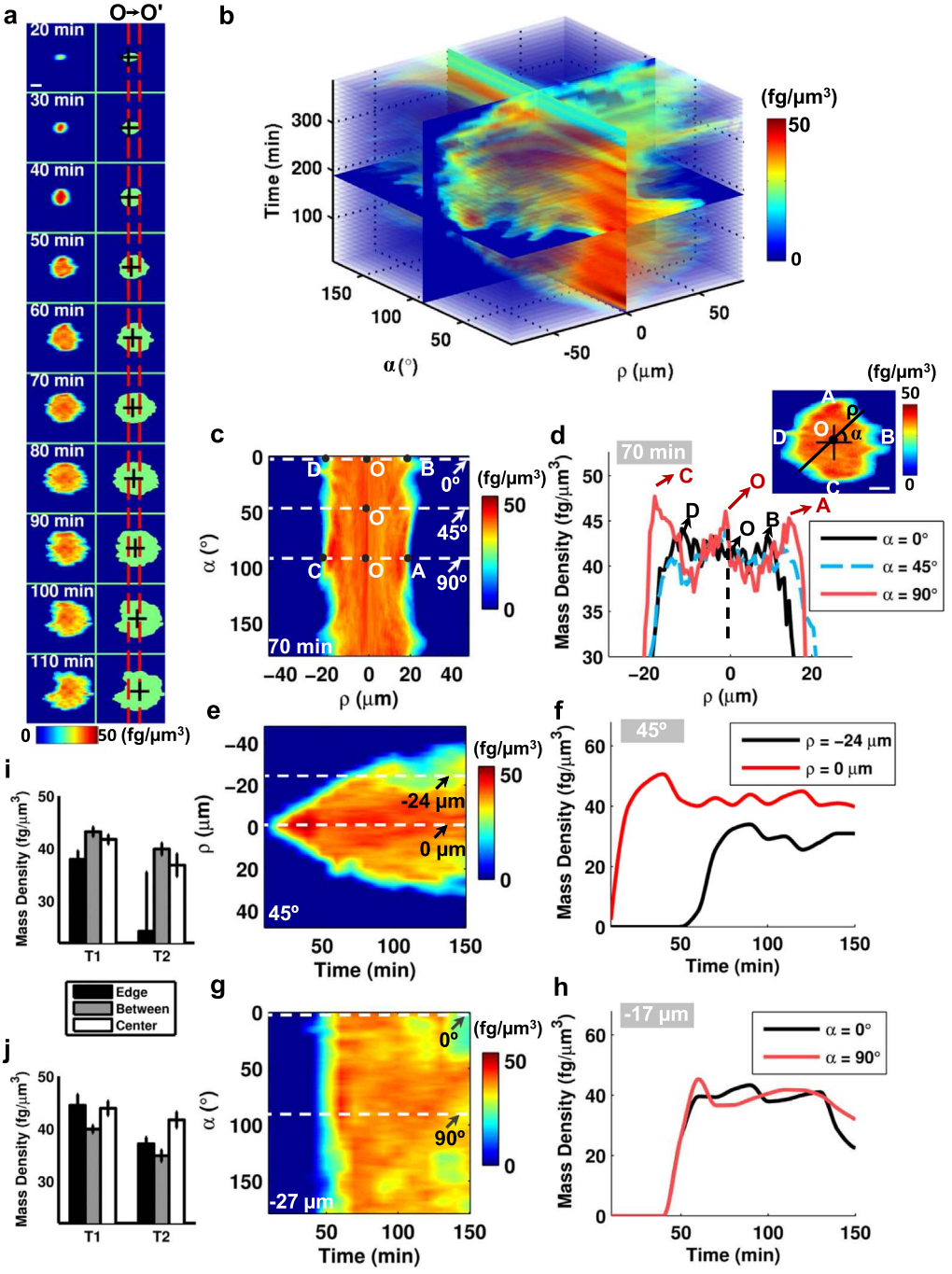

Fig. 5. *Stem Cell Edge-center Analysis Based on PCEM Images.* (a) The centroid of a live stem cell (mHAT) is dynamically detected along the membrane-associated effective mass density image sequence. (b) The 3D spatiotemporal map re-sampled along the radial direction (diameter ρ and angle α) and time dimension (T) of a sequence of membrane-associated effective mass density images (unit: fg/μm^3). (c,e,g) depict the 2D Spatiotemporal ρ-α Maps (unit: fg/μm^3) extracted from the 3D maps in (b). (d,f,h) represent the 1D cross-section curves extracted from the 2D maps in (c,e,g). The statistical analysis at different locations (Edge, Center, in Between) inside the cell at two different time points (T1=50 min and T2=160 min) for two different re-sample angles: (i) α=0°, (j) α=90°. Bar length=10 μm.

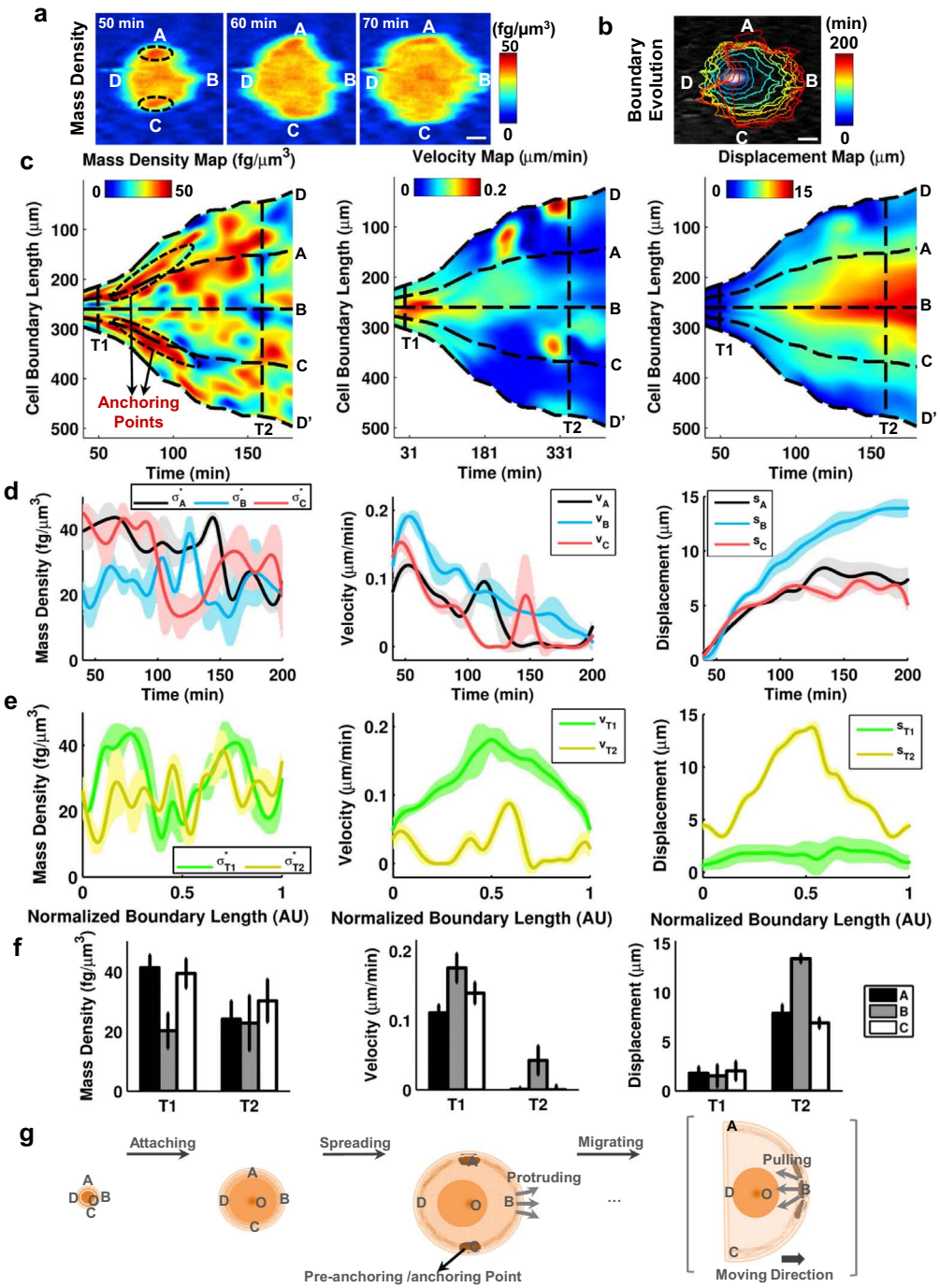

Fig. 6. *Label-free Imaging of Stem Cell Adhesion and Dynamic Traction of Boundary Evolution Using PCEM.* (a) Membrane-associated effective mass density (MD) images of three sequential frames of one stem cell (mHAT) (unit: fg/μm^3). (b) Detected cellular boundaries for a live cell at different frames (unit: minutes). (c) Re-sampled 2D spatiotemporal maps: Left: effective mass density map (unit: fg/μm^3); Middle: cell boundary velocity map (unit: μm/min); Right: cell boundary displacement map (unit: μm). (d) 1D cross section curves of above 2D maps along *temporal* dimension. (e) 1D cross section curves of above 2D maps along *spatial* dimension (with normalized cell boundary). (f) Statistical analysis at different locations (A,B,C) along the cell boundary. (g) Hypothesis of earlier status of cell adhesion and migration supported with anchoring points. First, cell is attaching to the substrate surface. Then, cell is anchoring with two sides of the body as supporting points and protruding the frontier parts toward the moving direction. Finally, after adhesion process, cell is migrating toward the moving direction by pulling the whole body with the frontier. Bar length=10 μm.

surface attachment profiling can be easily extracted from PWS images, and cannot be obtained from conventional brightfield images.

Using the conversion method from PWS to effective mass density, we obtain the images of cell membrane-associated effective mass density (MD) shown in Fig. 4 and S-Figs. 2–3. Fig. 4a and S-Fig. 2 demonstrate the initial adhesion process for three different

mHAT cells (imaged at a time interval of 10 s/frame for short term imaging of 0~30 min) and Fig. 4b plots the mean and standard deviation (std) values (N=6 cells) of the membrane-associated effective mass density, which is increasing at a rate of ~6.03 fg/(μm^3 min) during adhesion. Fig. 4c–f and S-Fig. 3 demonstrate the repeated drug responses of mHAT cells (N=9 cells) treated with Trypsin (Sigma-Aldrich, Co. LLC.) for different concentrations and incubation times (imaged at interval of 2 min/frame for long term imaging of 0~25 h). As shown in Fig. 4d and f (kinetics curve-fitting of drug responses see Methods Section 4.3.3 for details), the average membrane-associated effective mass density decreases at a rate of ~8.73 fg/(μm^3 min) for high concentration (0.025%), and ~2.04 fg/(μm^3 min) for low concentration (0.0025%), respectively. After washing out the Trypsin, the membrane-associated effective mass density increases at a rate of ~0.65 fg/(μm^3 min) for short term incubation (~10 min) with high Trypsin concentration, and ~5.43 fg/(μm^3 min) for long term incubation (~20 min) with low Trypsin concentration. These quantitative measurements of dynamic local membrane-associated effective mass density change of live cells in response to drug exposure can be broadly applied to numerous pharmaceutical and biological research areas.

2.3. Dynamic tracking of local membrane-associated effective mass density during cell adhesion

Image analysis software has been developed in Matlab (Matlab, Mathworks, Inc.) to dynamically track cell boundary evolution and to quantify local membrane-associated effective mass density changes (Figs. 5 and 6, movie 1). For example (Fig. 5a), the centroid (geometric center) of a mHAT cell (O) can be tracked (black cross marked on the right column) in the sequence of PCEM images and the movement of the cell center (O= > O′) demonstrates that the attached cell center migrates towards a specific direction. The estimated average velocities at attached cell center (from 90~110 min) are ~0.190 μm/min along the horizontal direction (towards the right) and ~0.193 μm/min along the vertical direction (towards the top). Another analysis tool provided by the imaging software is shown in Fig. 5b. The 3D spatiotemporal map is obtained by resampling the membrane-associated effective mass density image sequences of the same mHAT cell along the radial direction (diameter ρ and angle α, cross the dynamical cell center O) and time dimension (T). The resulting map can be utilized to analyze the center-edge relationship for distribution and redistribution of attached cellular materials. The corresponding 2D slices extracted from the 3D map can be employed to examine the local change along multiple combinations of axes, including ρ-α (Fig. 5c), T-ρ (Fig. 5e), T-α (Fig. 5g). For instance, the 2D ρ-α map at T=70 min (Fig. 5c) depicts a membrane-associated effective mass density sinogram sampled along the radial direction. The vertical band near center (around ρ=0 μm) shows high effective mass density along all angles, which indicates that cell center may show stronger interactions with the substrate along all radial directions. On the other side, the vertical bands near the cell edge (around ρ=−20 μm and ρ=20 μm) demonstrate high amplitudes only at two areas (from α=~70° to α=~110°), which is at the top (around point A) and bottom (around point C) of the cell, and this pattern of effective mass density distribution (high center and high partial edge) is especially obvious around T=50~60 min. This trend is further confirmed by plotting the 1D ρ curves (Fig. 5d, red curve) extracted from the 2D ρ-α map, which represent the membrane-associated effective mass density sampled along the radial direction with constant angle at a specific time point. The red curve in Fig. 5d represents the membrane-associated mass density sampled at α=90° and the three peaks (marked with A, O, C) on the curve indicates high local membrane-associated mass density at cell center (O) and edges (A, C) at T=70 min. The quantitative images provide insights into cell behavior: at the earlier stage of cell-surface interactions, the cell may use some specific areas (such as the center or two sides of the cell body) as pre-anchoring/anchoring points to support the whole body adhesion or migration. Combined with the prior knowledge of the cell center migration direction (towards the right) obtained from Fig. 5a, another insight is that the cell pre-anchoring points may not localize at the leading edge of the cell (as commonly assumed) at the earlier adhesion stage. Distinguished from the focal adhesion sites typically observed in the frontier of the cell body during mature adhesion and migration, these pre-anchoring/anchoring points seem to form quickly and last only briefly, and may not always be located in the leading edge of the cell. Similar cellular behaviors have been seen during neutrophil rolling on substrate surfaces [13].

Supplementary material related to this article can be found online at: http://dx.doi.org/10.1016/j.pquantelec.2016.10.001.

More complex information can be extracted from local membrane-associated effective mass density images in both temporal and spatial dimensions (Fig. 6). As shown in Fig. 6a–b, the mHAT cell boundary can be tracked (along local normal direction to the cell boundary at each pixel) and membrane-associated effective mass density images can be sampled along the cell boundary spatially and temporally (see Methods Section 4.3.4 for details) [50]. The resulting 2D spatiotemporal maps (Fig. 6c) represent the attached cellular membrane-associated effective mass density (Left), cell boundary velocity (Middle), and total displacement (Right) at each sampling window along the cell plasma membrane and time frames, respectively. From these spatiotemporal maps, many interesting phenomena can be observed and more obviously highlight specific aspects of cell adhesion behavior with quantitative measurements. One representative case is presented here as an example of cell attachment and simultaneous anchoring, as a mHAT cell prepares for future migration on a fibronectin coated PC biosensor surface. The mean and standard deviation of the cross section curves, selected from three different boundary locations (A,B,C in Fig. 6a) in three maps, are plotted in Fig. 6d along the temporal dimension. They indicate that the attached cellular membrane-associated mass density exhibits high amplitude at the two sides (near points A and C) of the cell body (σ_A* and σ_C*) at an early adhesion stage (e.g. 40~110 min), and then slightly decreases. Simultaneously, the cell boundary, especially at the right side of the cell body (near point B), moves towards the right, with the velocity (V_B) initially high but decreasing with time (Fig. 6d, Middle), sharing the same trend (decreasing) as the membrane-associated effective mass density change (σ_A^* and σ_C^*) (Fig. 6d, Left) (the curves are plotted together in S-Fig. 4 for timing comparison). The accumulated changes in the velocity can also be observed as a delayed increase in the cell boundary moving distance (S_B) (Fig. 6d, Right). Furthermore, the decrease in the velocity (V_B) can be verified from the cross section curves (V_{T1} and V_{T2}) selected along the spatial dimension with normalized boundary length (Fig. 6e, Middle). In addition, statistical analysis can be performed on PCEM data, and one example is

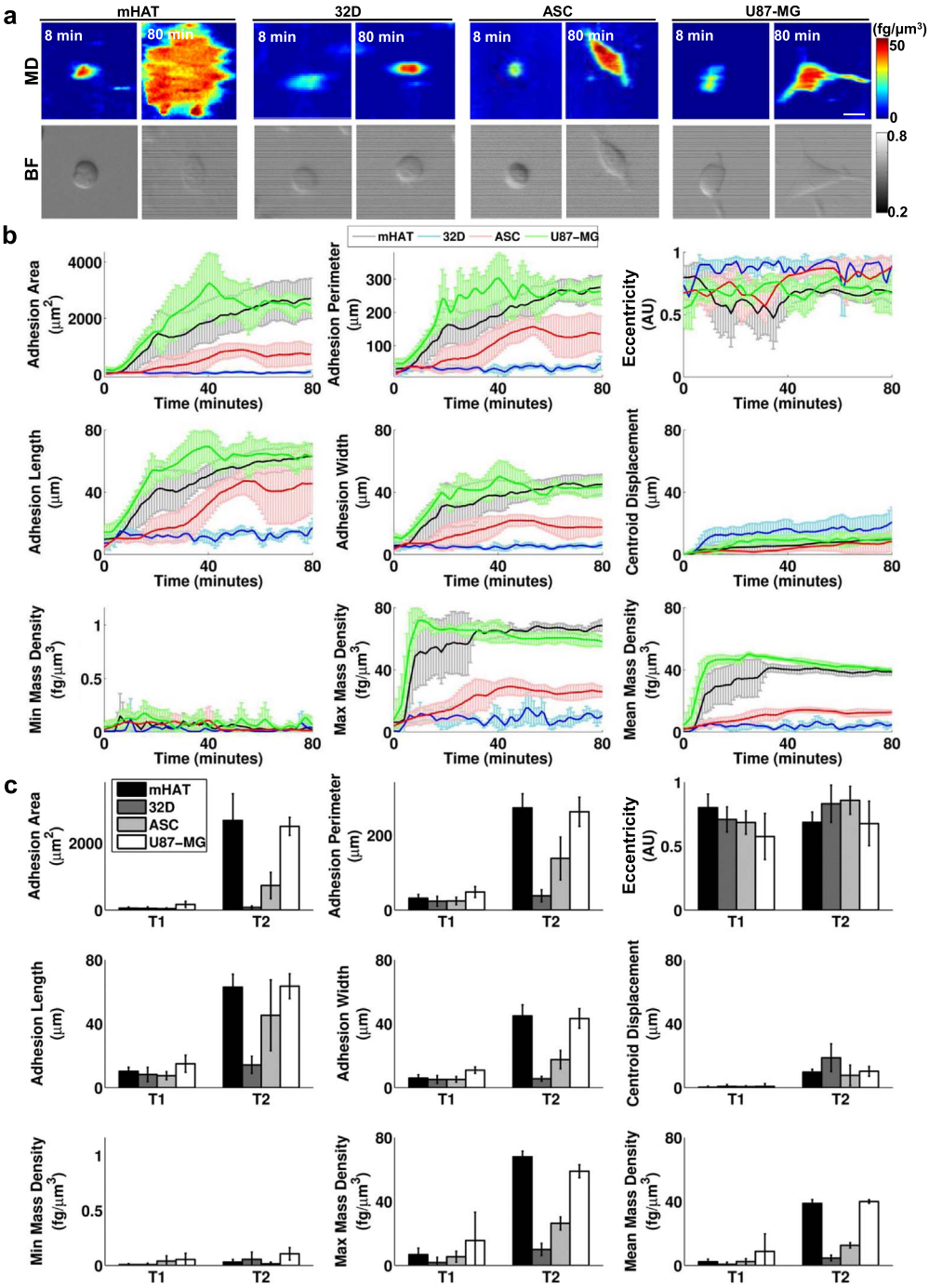

Fig. 7. *Effective Mass Density Images Representing Measurements and Statistical Analysis From Different Stem Cells and Cancer Cells.* (a) Membrane-associated effective mass density (MD) images of three different types of stem cells and one type of cancer cells: mHAT (dental stem cell), 32D (myeloid stem cell), ASC (adipose stem cell), U87-MG (brain cancer cell). Statistical comparison of attached cellular materials for different types of cells, including eccentricities, attached cellular areas/perimeters/length/width/centroid displacement, and min/max/mean effective mass density values (N=5 cells for each type): (b) plots the mean and standard deviation along time dimension (0~80 min); (c) represents at two different time points (T1=8 min, T2=80 min). Bar length=10 μm.

shown as the mean and standard deviation estimated through the entire boundary, frame-by-frame, along the temporal dimension (Fig. 6f). Interestingly, the corresponding integration over the whole cell area (cell membrane-associated effective *mass* distribution) for the entire boundary along the temporal dimension (S-Fig. 5b) shows a trend (increasing) opposing the trend (slightly decreasing) observed in the mean and standard deviation analysis of the cell membrane-associated effective *mass density* distribution (S-Fig. 5a). This may be explained by the fact that the cell is mainly *spreading* at the earlier stage (after attaching to the substrate), so

the cellular membrane-associated effective *mass density* is initially concentrated in a small spherical volume and then decreases, although the overall surface attached effective *mass* increases due to the increase in the overall contact area. This statistical evaluation can be used to develop a cell attachment model, which may help to further uncover the underlying mechanism of active sensing of the micro cellular environment (e.g. cell-ECM interaction), activation of cytoskeleton molecules (e.g. polymerization of microtubule or actin filaments) and transmembrane receptors (e.g. integrins). From the above analysis, an early-stage cell adhesion/migration model can be considered, as shown in Fig. 6g. When a cell is actively binding and attaching to a substrate surface, it may first initialize some *pre-anchoring sites* (e.g. points A and C) to support the whole cell-body's protrusion in the moving-frontier (point B) in order to prepare for subsequent migration in a specific direction. After protrusion, the cell moving frontier may pull the rest of the cell body to follow. It is noteworthy that the cell often needs some pre-anchoring/anchoring points distributed near the cell center (O) and nonleading edges (A,C) to support/prepare for the future whole body movements.

2.4. Cell adhesion phenotype library

An attractive application for PCEM is to build a quantitative cellular library with dynamic adhesion phenotypes for a wide range of attachable cells, which will be invaluable for cellular identification, classification, labeling, and other biosensing uses. Fig. 7 illustrates a small sample (N=5 cells for each type) of this library as a proof-of-concept with three different types of stem/progenitor cells (mHAT, 32D, and ASC) and one type of brain cancer cell line (U87-MG). In their undifferentiated state, these cells display morphologies distinct from each other: large, spread-out, rounded shape (mHAT); small, round shape (32D); elongated, spindled shape (ASC); and star-like shape (U87-MG). Fig. 7a plots the effective mass density (MD) and brightfield (BF) images measured with PCEM for these four types of cells in the beginning (~8 min) and end (~80 min) of the adhesion process, which clearly demonstrates adhesion features that are very distinct with respect to their cellular types. As shown in Fig. 7b with mean and standard deviation values of adhesion parameters, mHAT cells [51] (in gray) are a murine dental epithelial stem cell line differentiates to form an epithelium, and they tend to adhere tightly onto a PC substrate (e.g., high intensity of effective mass density ~40 fg/μm^3), spread rapidly with large adhesion areas (e.g., spread from ~10 μm^2 to ~3000 μm^2), and exhibit low adhesion eccentricities (e.g., ~0.6, which means that the cell morphology is more round compared to the other three types). 32D cells [52,53] (in blue) are a murine interleukin-3 (IL-3) dependent myeloid progenitor cell line that is widely used as an in vitro model of hematopoiesis as they spontaneously differentiate to granulocytic neutrophils upon the removal of IL-3 and introduction of granulocyte-colony stimulating factor (G-CSF) in the culture media. As with many types of hematopoietic cells, 32D cells are not anchorage-dependent cells and regarded only very weakly adherent, rendering adhesion phenotyping of these cells very challenging. PCEM, however, could parse out attachment and adhesion patterns for 32D cells with high spatial and temporal resolution. As expected with non anchorage-dependent cells, 32D cells demonstrate only weak adhesion (e.g. low intensity of effective mass density ~5 fg/μm^3) possibly due to high motility (e.g. high centroid displacement ~20 μm in 80 min), and nearly non-spreading adhesion area (e.g., ~100 μm^2). Porcine adipose-derived stem cells (ASC) [54,55] (in red) can differentiate to adipogenic, osteogenic, and chondrogenic lineages, and they form a spindle shape in their undifferentiated state, with middle-scale adhesion areas (e.g. ~1000 μm^2), high eccentricities (e.g. ~0.9, which means the cell is more elongated), and middle-scale mass density (e.g., ~15 fg/μm^3) on a PC surface. Finally, U87-MG cells [56] (in green) are a human primary glioblastoma cell line derived from malignant gliomas and widely used as an in vitro model to study glioblastoma multiforme (GBM), which is the most common and most aggressive form of brain cancer with rapid, diffuse infiltration, and is responsible for low patient survival rates that have remained unchanged for decades. U87-MG cells show star-like morphology with multiple spindles (high eccentricities of ~0.8), and rapidly spread to a relatively large adhesion area (e.g., spread from ~10 μm^2 to ~2000 μm^2) while showing tight adhesion (e.g., high intensity of effective mass density ~40 fg/μm^3). Statistical information (Fig. 7c) extracted from the curves in Fig. 7b at the beginning and end of the adhesion process (T1=~8 min, T2=~80 min) successfully quantifies and characterizes the unique dynamic adhesion phenotypes of these four types of cells. Such quantitative phenotyping information of dynamic cell adhesion can be utilized to study the mechanisms of cell-substrate interactions, as well as offering a novel means to identify cell populations based on their adhesion profiles, possibly opening up new avenues for bioengineering applications in vitro.

3. Conclusions

To summarize, PCEM can dynamically monitor and quantitatively measure cell-surface interactions and cellular membrane-associated effective mass density transport behavior with high sensitivity, high axial spatial resolution, and sufficiently high lateral spatial resolution to clearly observe attachment feature evolution within individual cells. PCEM is a new tool for measuring single-cell behavior that may hold great potential for studying cell-surface attachment profiles, cell-substrate interactions and cell-drug responses. As a label-free biosensor imaging approach, PCEM is capable of long term monitoring of live cells without applying cytotoxic stains or photobleachable fluorescent contrast agents in a cell-culture environment. In this work, we demonstrate the capabilities of PCEM that highlight the ability to observe the initial point of cell adhesion and the evolution of adhesion profiles in the spatial and temporal dimensions. PCEM data allow the constructions of new dynamic cellular membrane-associated effective mass density transportation models, which can estimate and predict movement of surface attached cell membranes and their related protein components, is fundamental for understanding and uncovering cellular regulation mechanisms. PCEM data can also potentially provide unique information for building cell adhesion and cell-substrate interaction models with subcellular detail. By gathering similar information for multiple cell types, ECM materials, and environmental conditions, our goal is to use PCEM to enable the construction of a "quantitative live cell footprint library" and provide a useful resource for biomedical and biomaterial research.

4. Methods and materials

4.1. Photonic crystal (PC) slab biosensor

4.1.1. PC slab biosensor resonance condition

A PC is an optical nanostructure-material with periodic modulation of its refractive index. Photonic crystal structures can be used as label-free biosensors since they enhance the light-matter interaction by providing localized resonant modes. A quasi-3D PC slab biosensor (stack of two layers of 1D PC slabs) is utilized in this work, in which a periodic modulation of the refractive index occurs in one direction only (e.g. x), while the material is uniform in another direction (e.g. y) and a stack in the third direction (e.g. z), as shown in Fig. 1a. For each 1D PC slab, the photonic eigen-modes for a Helmholtz equation can be expressed as combining Maxwell's equations with the source-free Faraday's and Ampere's laws at a given frequency:

$$\nabla \times \frac{1}{\boldsymbol{\varepsilon}} \nabla \times \mathbf{H} = \left(\frac{\omega}{c}\right)^2 \mathbf{H}, \tag{1}$$

where $\boldsymbol{\varepsilon}$ represents the periodic dielectric permittivity function and $(\nabla \times \frac{1}{\varepsilon} \nabla \times)$ is a Hermitian eigen-operator; ω denotes the desired angular frequency, c is the speed of light in free space (e.g. vacuum), and $(\omega/c)^2$ represents the eigen-value; the magnetic field $\mathbf{H}$ describes the eigen-functions; and the objective here is to solve for eigen-functions of a specific periodic structure and corresponding eigen-values.

Typically, the PC slab biosensor used in this work can be viewed as an infinite periodic structure since the period is in the submicron scale (e.g., ~400 nm) and the overall dimension of the biosensor is in the millimeter scale (e.g., ~9 mm), which indicates that the number of periods is more than three or four orders of magnitude. Based on the Bloch-Floquet theorem, eigen-functions of an infinite periodic structure can be represented by a plane wave multiplied by a periodic function with periodicity of the photonic lattice as:

$$\mathbf{H}(\mathbf{r}, t) = e^{i(\mathbf{k}\cdot\mathbf{r}-\omega t)} \mathbf{H}_0(\mathbf{r}), \tag{2}$$

where $\mathbf{r}$ is the spatial vector; t represents time; $\mathbf{k}$ is the wave vector; and $\mathbf{H_O}(\mathbf{r})$ is a periodic function with periodicity $\boldsymbol{\Lambda}$ of the photonic lattice of PC slab biosensor structure. Substitution of Eq. (2) into (1) yields the momentum-matching condition (or resonance condition) for the incident light coupling to the discrete in-plane guided mode supported by the periodic structure. Therefore, the resonance condition in each 1D photonic crystal slab can be described by the Bragg coupling equation:

$$\mathbf{k}_m = \hat{x}|\mathbf{k}_0|\sin(\theta) \pm \mathbf{G_x}, \tag{3}$$

where $\mathbf{k_m}$ is the wave-vector in a specific guided resonant mode; $\hat{x}$ represents the unit vector in x direction; $\mathbf{k_O}$ is the wave-vector of the incident wave ($|\mathbf{k_O}|=\frac{2\pi}{\lambda_0}$, where λ_0 is the wavelength of the incident light); θ is the launch angle of the incident light; and $\mathbf{G_x}$ is the photonic reciprocal lattice vector ($|\mathbf{G_x}|=m\frac{2\pi}{\Lambda}$, where m is the diffraction order of the resonant modes). As shown in Figs. 1a and i and 2b, for a given launch angle and grating period, the resonance wavelength can be tuned due to variation of the propagation constant induced by changing the refractive index of the surrounding media atop the PC slab. The resonance condition can provide guidance to the optical design for PCEM, such as θ=0° is chosen as normal incidence in this work (for simplification of imaging system), and $\boldsymbol{\Lambda}$=400 nm is chosen to realize the desired resonance wavelength λ_0=625 nm.

4.1.2. PC slab biosensor modeling

The PC slab used in this work has been previously described as a 1D PC slab nano-structure [43], which is slightly over-simplified. More strictly, this PC slab structure can be viewed as a quasi-3D nano-structure model (Fig. 1a), which can be decomposed into two layers of 1D PC slabs (if ignoring the side-wall effect). As shown in Fig. 1c–h, the Nanoslit (Top-PC-slab only, Fig. 1c and f) and Nanorod (Bottom-PC-slab only, Fig. 1d and g) have their own resonance conditions, which are both different from the resonance condition when the interference takes place in between (hybrid PC slabs with both top and bottom, Fig. 1e and h). As the white dotted lines indicate in Fig. 1c–e, the resonant peak wavelength at normal incidence angle is ~597 nm, ~604 nm, and ~625 nm for above three nano structures, respectively, when the background refractive index is close to that of water (n_{water}=~1.333). Besides, the highest normalized near-field intensity ($|E/E_0|^2$) of the evanescent field also takes place in the hybrid PC slab (Fig. 1h, Right Inset) among above three nano structures, which indicates again that the strong interference between two 1D PC slabs influences the total near-field intensity.

4.1.3. PC slab biosensor design

The peak wavelength is tunable by modifying the geometry of the PC slab due to altering the resonance conditions. To design a PC slab biosensor for imaging the cell adhesion in PCEM, understanding the individual effects of each geometry parameters is essential. For example, three important geometry parameters are marked in the diagram of the PC slab in Fig. 1a: grating period (Λ), grating height (D), and thickness of top high-RI layer (L). The effects of these three parameters on the peak resonance wavelength are plotted in Fig. 1i–n. For each layer of the PC slab (Top-only or Bottom-only), the grating period (Λ) can alter the distance of the optical path for the Bragg mirror, and results in a nearly linear relationship with the peak resonance wavelength in the hybrid PC slabs (Fig. 1i and l). The thickness of top high-RI layer (L) is related to the cavity length of the vertical Fabry–Pérot nanocavity and therefore also influences the location of the peak resonance wavelength (Fig. 1j and m). Finally, the grating height (D) affects the

interference between two layers of PC slabs and thus also influences the peak resonance wavelength (Fig. 1k and n). One of the critical aspects when designing the PC biosensor is to ensure the highest signal-to-background ratio (SBR) in reflectivity efficiency, which means that the reflectivity efficiency is high at the location of peak resonance wavelength and low at the other wavelengths. This can clearly be seen on Fig. 1i, j and k, which shows the peak resonance wavelength (in yellow) surrounded by the low background (in dark-red or nearly black).

4.1.4. PC slab biosensor simulation

A numerical simulation package (FDTD, Lumerical Solutions, Inc.) is used to calculate the distribution of excited electromagnetic fields on the PC slab biosensor surface. As shown in Fig. 1c–n and Fig. 2b–d, the simulation results predict the optimal physical parameters for the PC nano structure. A 1D UV-curable polymer structure (n_{UVCP}=~1.5) is utilized with a grating height (D=~120 nm) to confine the near field emission intensity. The grating period (Λ=400 nm) and duty cycle (f=~50%) of the PC slab biosensor are chosen to support resonant modes at wavelength of λ_O=~625 nm. The thickness (L=~81 nm) of the deposited high refractive index layer (TiO_2, n_{TiO2}=~2.4) is used to fine-tune the spectral location of the resonant modes. The corresponding evanescent-field is calculated as an average penetration depth of h_O=~62 nm into the surrounding media.

4.1.5. PC slab biosensor fabrication

A nanoreplica molding approach is used to fabricate the nano grating structure of the PC slab at room temperature, and can be fabricated on a plastic or glass substrate (glass substrate has been chosen in this work). As shown in Fig. 2a, a quartz master wafer with a negative volume image of the desired nano-grating structure is initially fabricated with E-beam lithography and Reactive Ion Etching (RIE) as the molding template. The liquid UV curable polymer (UVCP) is deposited between the wafer template and glass substrate. After exposure to high intensity UV illumination at room temperature for a short time (e.g. a couple of minutes), the UVCP is cured to a solid material with a replicated shape of the nano-structure of the molding template. After peeling off the master wafer, the nano-patterned surface is transferred to the glass substrate through UVCP. Then a thin layer of high-RI material (TiO_2) is deposited (e.g. with reactive RF sputtering machine, PVD 75, Kurt J. Lesker, PA) atop the nano-grating structure. Fig. 2i shows an SEM image of the fabricated PC slab surface (Inset: Photo of fabricated PC slab surface on a glass substrate).

4.1.6. PC slab biosensor characterization

The fabricated PC slab surface is characterized by a linear optical transmission/reflection setup with illumination of collimated and p-polarized white light. A mixture of DMSO and water solution with different effective refractive indices were prepared and exposed to the PC slab surface. The results demonstrate that high spectral resolution for quantifying RI changes in the reflected resonant wavelength from the PC slab surface can be realized due to the narrow spectral response (Fig. 2e–h). The resonance wavelength (λ_0) of the PC is tuned by varying the RI of background materials (within the evanescent field region) at different incident angles. The simulated and experimental 2D dispersion maps are shown in Fig. 2b,e, and the imaging experiments in this work were performed with resonant wavelength of λ_0=~625 nm at normal incident angle (θ=0°). The narrowband reflectance behavior is predicted by FDTD simulation (Fig. 2c) and verified by experiment with FWHM of ~3.6 nm (Fig. 2f). The sensitivity curve estimated from the simulation and experimental data is plotted in Fig. 2d and g.

4.1.7. PC slab biosensor surface preparation for bio-experiment

The PC slab biosensor is cleaned by sonication in isopropyl alcohol (IPA) and in deionized (DI) water for one minute each, followed drying with nitrogen (N_2) gas. Then the PC slab biosensor is oxygen-plasma treated to further clean and facilitate attachment of a liquid containment gasket formed from polydimethylsiloxane (PDMS). Finally, the PC slab surface is hydrated with phosphate buffered saline solution and coated with a layer of arbitrary ECM (e.g. fibronectin) to promote cellular attachment.

4.2. Photonic Crystal Enhanced Microscope (PCEM)

4.2.1. PCEM principle and design

The PCEM instrument is a modified brightfield microscope that uses a line-scanning approach to measure the spatial distribution of PWV across a PC slab surface with submicron spatial resolution for label-free imaging (Fig. 3) [42,57]. As shown in Fig. 3e, a light emitting diode (LED) is used as the non-coherent light source, and the line profiled and p-polarized (perpendicular to the nano-grating structure) light beam illuminates the PC slab biosensor from below (which eliminates scattering or absorption from materials in attached cell bodies) through a microscope objective lens. The reflected light, containing the resonant reflected spectrum, passes through the objective lens in the opposite direction, and is passed through the entrance slit of an imaging spectrometer, which records the resonant reflected spectrum from each voxel across the illuminated line on the PC slab. High spatial resolution in the axial direction is obtained due to the shallow evanescent-field on the PC slab surface. Spatial resolution in the lateral direction is determined by the lateral propagation distance of resonant coupled photons, resulting in detection of distinct surface attached objects for widely dispersed features at the 10~100 nm size scale [43]. Small nonuniformities may appear in the PWV background of as-fabricated PCs during imaging due to, for example, slight nonuniformity in the deposited TiO_2 thickness during the PC slab fabrication process. To eliminate the nonuniform background, we subtract the initial PWV of the blank PC slab immersed in cell media (before cell attachment) from the PWV (after cell attachment) on a voxel-by-voxel basis to generate the PWS images that are reported here. When a cell attaches to the PC surface (Fig. 3a–d), the peak resonant wavelength red-shifts from a lower wavelength (before cell attachment, e.g. λ_O=~625 nm) to a higher wavelength (after cell attachment, e.g. λ_{cell}=~627 nm). A positive PWS

indicates that the cell-media in contact with the PC slab surface with a low-RI (e.g. n_{water}=~1.333) is replaced by cellular materials with a greater-RI (e.g. n_{cell}≈1.35~1.38). As higher densities of membrane components and intracellular protein components of cell membranes associated with focal adhesions are recruited to the PC slab surface, the magnitude of the local RI will increase. Therefore, the PWS image represents the effective mass density distribution of cell components that engage the PC slab surface.

4.2.2. PCEM imaging system implementation

The PCEM imaging system is integrated with an ordinary inverted light microscope (Carl Zeiss Axio Observer Z1). The non-coherent light is emitted from a LED (Thorlabs M617F1), and line-profiled with a cylindrical lens and p-polarized with a polarized beam splitter (PBS), then illuminated from beneath the PC slab biosensor for live-cell imaging (Fig. 3e). A motorized translation stage (Applied Scientific Instruments, Inc.) is used to perform the line-scan. A charge-coupled device (CCD) camera (Photometrics Cascade 512) combined with an imaging spectrometer (Acton Research) is utilized to collect the spectral data for each voxel. For the spatial resolution of the PCEM system, the leaky mode propagation in the photonic crystal influences the resolution in the lateral direction. It had been previously established [43] experimentally and with the support of computer models that the lateral distance at which a point source (TiO_2 nanoparticles (n_{TiO2}=2.4~2.5) and printed polymer nanodots (n_{poly}=~1.5)) of high refractive index contrast effects neighboring regions on the PC (n_{water}=~1.333) is approximately 2 microns for the structures used in this paper. However, the refractive index contrast between a loci of cell attachment within a cell membrane (n_{cell}≈1.35~1.38) and the surrounding media (n_{water}=~1.333) will be less than these discrete test objects. In our PCEM images, we observe strong contrast in the reflected wavelength at cell boundaries and within the cells themselves from one pixel to its neighbor, and thus the lateral contrast is likely similar (or can be approximated) to the ~600 nm pixel size. Therefore, as shown in Fig. 3e–f, the voxel dimension at each spatial location is δV=~0.6^2×0.062 μm^3 which is mainly determined by: (a) the magnification of the objective-lens (e.g. 10×) and the pixel size of CCD camera in x direction (perpendicular of grating in lateral direction), (b) the magnification of the objective-lens and step-size of the imaging translation-stage in y direction (parallel of grating in lateral direction), and (c) the penetration depth of the evanescent-field in z direction (axial direction). For the temporal resolution of the PCEM system, the shortest time between successive PCEM images is determined by a combination of factors that include: (a) Mechanical: the speed of the motorized stage to return the PC biosensor to its origin pre-scan location and the size of the scan area, (b) Optical: exposure time of camera required to gather each line of the image, for the purpose of gathering a low-noise resonant reflection spectrum. In the present PCEM system, the exposure time per line is ~50 μs, which is mainly determined by the intensity of the ~4.4 mW broadband illumination source (e.g., LED).

4.3. PCEM data analysis

4.3.1. Peak wavelength value (PWV) extraction

Image-analysis software is developed with computational software (Matlab, MathWorks) to process the PCEM acquired 3D spectra data (e.g., 512^3 voxels). The spectrum at each voxel is smoothed using a low-pass filter to reduce acquisition noise and then fitted to a 2nd order polynomial to extract the maximum wavelength value (referred to as peak wavelength value (PWV)). Based on the PWV/PWS data, a kinetics curve-fitting program for cell adhesion and drug-response (Fig. 4), a cell edge-center analysis program (Fig. 5), and a cell boundary extraction and motion traction program (Fig. 6) are implemented to extract the cell-attachment induced local membrane-associated effective mass density change.

4.3.2. Converting peak wavelength shift (PWS) map to effective mass density (MD) map

Typically, refractive index n depends on the light wavelength and the material density probed by the light [46–48]. When the change of refractive index is small, it can be approximated as linearly proportional to the shift of resonance wavelength at each voxel location on the PC slab surface (Fig. 2c, d, f and g). Therefore, the local refractive index map can be obtained (Fig. 2h) from the PWV maps with the prior knowledge measured from adding incremental amount of proteins.

Refractive index represents the optical density of the material, which is not the same as the physical density (though related with each other in certain level). If each protein can be viewed approximately as a dipole, not only the physical density, but also the polarization of the dipole moment in the incident light field will influence the vibration of electrons. However, the speed of a light wave is dependent upon the properties of the propagation medium. It means that in the case of an electromagnetic wave, the speed of the wave depends upon the optical density of the material. The physical density of a material refers to the mass/volume ratio. The optical density of a material relates to the tendency of the atoms of a material to maintain the absorbed energy of an electromagnetic wave in the form of vibrating electrons before reemitting it as a new electromagnetic disturbance. The more optically dense that a material is, the more slowly a wave will move through the material. One indicator of the optical density of a material is the index of refraction value of the material. Index of refraction values (represented by the symbol n) are numerical index values with arbitrary unit (AU) that are expressed relative to the speed of light in free space (e.g. vacuum). Therefore, the index of refraction value of a material is a number that indicates the number of times slower that a light wave would be in that material than in a vacuum.

It has been reported that the local effective mass density $\sigma^*(x,y,z)$ of a live cell can be estimated from the refractive index map through integrated phase shift with a nearly linear relationship [46–48]. When the electromagnetic wave propagates through cellular material, the integrated refractive index shift $\Delta n(x,y,z)$ in each voxel volume can be estimated as below [58]

$$n(x, y, z) = n_0 + \Delta n(x, y, z) \approx n_0 + \beta \cdot C(x, y, z), \tag{4}$$

where n_O is the initial refractive index of the surrounding cell culture media (assume homogenous); β (in unit of ml/g) is known as

the refractive increment and the typical value is ~0.19 ml/g in cellular material; $C(x,y,z)$ (in unit of g/ml) represents the change in concentration of protein molecules.

If the local incident wave can be approximated as a plane wave in each voxel volume on the PC slab surface, then the reflected wave can also be approximated as a plane wave with different resonance wavelength and phase. When the reflected plane wave propagates through the cellular material, the phase shift can be defined as

$$\Delta\phi(x, y, z) = k_0[n(x, y, z) - n_0] = k_0\Delta\bar{n}(x, y, z), \tag{5}$$

where $k_O=2\pi/\lambda_O$ is the initial wave number and λ_O is the initial peak wavelength of the incident light; $\Delta\bar{n}(x, y, z)$ is the refractive index contrast between the cellular material and the surrounding cell culture medium averaged in each voxel (laterally within the pixel area and axially through the evanescent field). Accordingly, the change of the effective local membrane-associated effective mass density at each voxel can be approximated as:

$$\Delta\sigma^*(x, y, z) \approx \frac{\lambda_0}{2\pi\beta}\Delta\phi(x, y, z) \approx \frac{\Delta\bar{n}(x, y, z)}{\beta}. \tag{6}$$

Note that the evanescent part of the electromagnetic field has been taken into account and this information is present as "z" in the 3D Eq. (6). Since the measured PWV is the "bulk value" in the 3D volume of the voxel on the PC surface, "z" can be represented by the average penetration length h_0 and thus automatically included in the Eq. (6). It implies that this analysis does not need to incorporate the local thickness of the attached cellular material within the sensing zone of the PC biosensor, though it can be approximated as the average penetration length h_O (estimated as ~62 nm in this work) of the evanescent field (the edge effect on the cell boundary is also ignored here). Thus, the local membrane-associated effective mass density can be directly estimated within a small volume (e.g., δV=~$0.6^2\times0.06$ μm^3) at each voxel. When the increment of the refractive index is small, the local effective mass density of a thin layer in the bottom of the attached cell body at each voxel is approximately linearly proportional to the change of refractive index (or resonant wavelength shift measured with PCEM) (as indicated in Fig. 2k).

4.3.3. Modeling cellular mass density transportation kinetics

1) Adhesion Kinetics

As shown in Fig. 4b, the dynamic cellular membrane-associated effective mass density $\sigma^*(t)$ (*mean* effective mass density for each cell within the adhesion area) can be modeled with the Generalized Logistic Function (GLF):

$$\sigma^*(t) = \sigma_b^* + \frac{\sigma_a^* - \sigma_b^*}{(1 + e^{(t_{half}-t)k_{sl}})^{1/v}}, \tag{7}$$

where σ_a^* and σ_b^* are the asymptote maxima (after adhesion) and asymptote minima (before adhesion) of effective mass density value, respectively; t is the time and t_{half} represents the time point at half maximum of effective mass density value; k_{sl} denotes the slope which reveals the steepness of the effective mass density curve when arising; v affects near which asymptote maximum of effective mass density curve occurs.

2) Drug Response Kinetics

As shown in Fig. 4d and f,

$$\sigma^*(t) = \sigma_b^* + \frac{\sigma_{a,1}^* - \sigma_b^*}{(1 + e^{-(t_{half,1}-t)k_{sl,1}})^{1/v_1}} + \frac{\sigma_{a,2}^* - \sigma_b^*}{(1 + e^{(t_{half,2}-t)k_{sl,2}})^{1/v_2}}, \tag{8}$$

where the symbols share similar meanings as in Eq. (7), except that the second and third terms represent the decreasing (after adding drugs) and increasing (after washing out the drugs) period of the effective mass density curve, respectively.

4.3.4. Cell adhesion boundary evolution traction

For dynamically tracking cell boundary evolution (Fig. 6) [50], we adapted the Level Set Method (LSM), which is an approach for tracking the evolution of complex boundaries. The following equation defines the location of cell boundary on the PC slab surface at a certain time:

$$\Gamma(t) = \{(x, y)|\varphi(x, y, t) = 0\}, \tag{9}$$

where $\Gamma(t)$ represents the cell boundary at time t; the point (x, y) is located at the cell boundary on PC slab surface; $\varphi(x,y,t)$ is the level set function, which represents the signed distance from location (x,y) to the boundary $\Gamma(t)$ at time t. Eq. (9) illustrates that the cell boundary $\Gamma(t)$ can be estimated at the zero level of the level set function $\varphi(x,y,t)$ at any time t. To simplify the calculation, we assume that the cell boundary moves toward its normal direction, and the cell boundary evolution thus can be described as a Hamilton-Jacobi equation:

$$\frac{\partial\varphi(x, y, t)}{\partial t} = V(\varphi(x, y, t), t)|\nabla\varphi(x, y, t)|, \tag{10}$$

where $V(\varphi(x,y,t),t)$ is the speed function of level set function $\varphi(x,y,t)$ at time t; ∇ represents the gradient operator; and $|\bullet|$ denotes the Euclidean norm. Eq. (10) depicts that the cell boundary $\Gamma(T)$ can be propagated to its consecutive frame boundary $\Gamma(T+1)$ using LSM through estimating the intermediate boundaries.

4.4. Cell culture

4.4.1. Cell culture condition

Similar to the environment of a general cell culture incubator, a customized chamber is built in PCEM system to cover the sample stage, and connected with the carbon dioxide (CO_2) mixer to provide 5% CO_2 air with humidity to maintain certain pH value of the cell medium (which is necessary to the long term live cell survival).

4.4.2. Cell culture

1) mHAT (murine dental stem cell): Stable cultures of mHAT cells were maintained in Dulbecco's Modified Eagle Medium (DMEM) supplemented with 10% fetal bovine serum (FBS) and 1% penicillin streptomycin (PenStrep).
2) 32D (myeloblast-like stem cell): Stable cultures of the 32D cells were maintained in Roswell Park Memorial Institute (RPMI) 1640 medium with 2 mM L-glutamine adjusted to contain 1.5 g/L sodium bicarbonate, 4.5 g/L glucose, 10 mM 4-(2-Hydroxythyl)-1-Piperazineethanesulfonic acid (HEPES), and 1.0 mM sodium pyruvate supplemented with 10% heat-inactivated FBS and 10% mouse WEHI-conditioned medium.
3) ASC (porcine adipose stem cell): Stable cultures of ASCs were maintained in low glucose DMEM supplemented with 10% FBS and 1% PenStrep.
4) U87-MG (human primary glioblastoma cell line): Cultures of U87-MG were maintained in DMEM supplemented with 10% FBS and 1% PenStrep.

Author Contributions

Y.Z. and J.C. designed the experiments, performed experiments and wrote the manuscript; Y.Z. and T.M. developed the analysis software and performed the data analysis; Y.Z. and H.Y. fabricated the PC sensors; B.C. and B.H. provided guidance and edited the manuscript.

Acknowledgements

This work is supported by National Science Foundation (NSF) Grant CBET 11-32301, National Institutes of Health (NIH) R01 DK099528 and NIH R21 EB018481. The content is solely the responsibility of the authors and does not necessarily represent the official views of the NSF and NIH. Porcine adipose derived stem cells were a gift from Dr. Mathew Wheeler in University of Illinois at Urbana-Champaign (UIUC). The authors would like to thank the members in Nano Sensor Groups (NSG) and Engineered Cellular Microenvironments and microstructures Lab (ECMLAB), staff in Micro and Nanotechnology Laboratory (MNTL) and Institute for Genomic Biology (IGB), the Center for Innovative Instrumentation Technology (CiiT) at UIUC for their discussion and support.

Appendix A. Supplementary material

Supplementary data associated with this article can be found in the online version at: http://dx.doi.org/10.1016/j.pquantelec.2016.10.001.

References

[1] R.B. Vallee, M.P. Sheetz, Targeting of motor proteins, Science 271 (1996) 1539–1544.
[2] F.C. Mackintosh, C.F. Schmidt, Active cellular materials, Curr. Opin. Cell Biol. 22 (2010) 29–35. http://dx.doi.org/10.1016/j.ceb.2010.01.002.
[3] G.S. Hillis, A.D. Flapan, Cell adhesion molecules in cardiovascular disease: a clinical perspective, Heart 79 (1998) 429–431.
[4] J.T. Parsons, A.R. Horwitz, M.A. Schwartz, Cell adhesion: integrating cytoskeletal dynamics and cellular tension, Nature Rev.. Molecul. Cell Biol. 11 (2010) 633–643. http://dx.doi.org/10.1038/nrm2957.
[5] Y. Alapan, J.A. Little, U.A. Gurkan, Heterogeneous red blood cell adhesion and deformability in sickle cell disease, Sci. Rep. 4 (2014) 7173. http://dx.doi.org/10.1038/srep07173.
[6] Y. Sun, C.S. Chen, J. Fu, Forcing stem cells to behave: a biophysical perspective of the cellular microenvironment, Annu. Rev. Biophys. 41 (2012) 519–542. http://dx.doi.org/10.1146/annurev-biophys-042910-155306.
[7] T. Hochstrasser, E. Weiss, J. Marksteiner, C. Humpel, Soluble cell adhesion molecules in monocytes of Alzheimer's disease and mild cognitive impairment, Exp. Gerontol. 45 (2010) 70–74. http://dx.doi.org/10.1016/j.exger.2009.10.005.
[8] F. Lanni, A.S. Waggoner, D.L. Taylor, Structural organization of interphase 3T3 fibroblasts studied by total internal reflection fluorescence microscopy, J. Cell Biol. 100 (1985) 1091–1102.
[9] B. Rothenhäusler, W. Knoll, Surface-plasmon Microscopy, Nature **332** (1988) 615–617.
[10] D. Axelrod, Total internal reflection fluorescence microscopy in cell biology, Traffic 2 (2001) 764–774.
[11] G. Popescu, et al., Optical imaging of cell mass and growth dynamics, Am. J. Physiol. Cell Physiol. 295 (2008) C538–C544. http://dx.doi.org/10.1152/ajpcell.00121.2008.
[12] B. Joshi, et al., Phosphorylated caveolin-1 regulates Rho/ROCK-dependent focal adhesion dynamics and tumor cell migration and invasion, Cancer Res. 68 (2008) 8210–8220. http://dx.doi.org/10.1158/0008-5472.CAN-08-0343.
[13] P. Sundd, et al., Quantitative dynamic footprinting microscopy reveals mechanisms of neutrophil rolling, Nat. Methods 7 (2010) 821–824. http://dx.doi.org/10.1038/nmeth.1508.
[14] S.P. Wang, et al., Label-free imaging, detection, and mass measurement of single viruses by surface plasmon resonance, Proc. Natl. Acad. Sci. USA 107 (2010) 16028–16032. http://dx.doi.org/10.1073/pnas.1005264107.
[15] K. Park, et al., Measurement of adherent cell mass and growth, Proc. Natl. Acad. Sci. USA 107 (2010) 20691–20696. http://dx.doi.org/10.1073/

pnas.1011365107.
[16] M.R. Gartia, et al., Colorimetric Plasmon Resonance Imaging Using Nano Lycurgus Cup Arrays, Adv. Opt. Mater. 1 (2013) 68–76.
[17] T.A. Zangle, M.A. Teitell, Live-cell mass profiling: an emerging approach in quantitative biophysics, Nat. Methods 11 (2014) 1221–1228. http://dx.doi.org/10.1038/nmeth.3175.
[18] T. Kim, et al., White-light diffraction tomography of unlabelled live cells, Nat. Photonics **8** (2014) 256–263.
[19] J. Jiang, et al., Large-area, lithography-free, low-cost SERS sensor with good flexibility and high performance, Nanotechnology 27 (2016) 385205. http://dx.doi.org/10.1088/0957-4484/27/38/385205.
[20] A. Hessel, A.A. Oliner, A New Theory of Wood's Anomalies on Optical Gratings, Appl.Opt. 4 (1965) 1275–1297.
[21] L. Mashev, E. Popov, Diffraction efficiency anomalies of multicoated dielectric gratings, Opt. Commun. 51 (1984) 131–136.
[22] E. Popov, L. Mashev, D. Maystre, Theoretical study of the anomalies of coated dielectric gratings, Opt. Acta 33 (1986) 607–619.
[23] E. Yablonovitch, Inhibited spontaneous emission in solid-state physics and electronics, Phys. Rev. lett. 58 (1987) 2059–2062.
[24] S. John, Strong localization of photons in certain disordered dielectric superlattices, Phys. Rev. lett. 58 (1987) 2486–2489.
[25] R.D. Meade, K.D. Brommer, A.M. Rappe, J.D. Joannopoulos, Electromagnetic Bloch waves at the surface of a photonic crystal, Phys. Rev. B 44 (1991) 10961–10964.
[26] R. Magnusson, S.S. Wang, New principle for optical filters, Appl. Phys. Lett. 61 (1992) 1022–1024.
[27] J.D. Joannopoulos, P.R. Villeneuve, S. Fan, Photonic crystals: putting a new twist on light, Nature 386 (1997) 143–149. http://dx.doi.org/10.1038/386143a0.
[28] S. Fan, P.R. Villeneuve, J.D. Joannopoulos, E.F. Schubert, High Extraction Efficiency of Spontaneous Emission from Slabs of Photonic Crystals, Phys. Rev. lett. 18 (1997) 3294–3297.
[29] M. Kanskar, et al., Observation of leaky slab modes in an air-bridged semiconductor waveguide with a two-dimensional photonic lattice, Appl. Phys. Lett. 70 (1997) 1438–1440.
[30] S.G. Johnson, S. Fan, P.R. Villeneuve, J.D. Joannopoulos, L.A. Kolodziejski, Guided modes in photonic crystal slabs, Physical Review B 60 (1999) 5751–5758.
[31] W.M. Robertson, M.S. May, Surface electromagnetic wave excitation on one-dimensional photonic band gap arrays, Appl. Phys. Lett. 74 (1999) 1800–1802.
[32] M. Boroditsky, et al., Spontaneous emission extraction and Purcell enhancement from thin-film 2-D photonic crystals, Lightwave Technol. 17 (1999) 2096–2112.
[33] O. Painter, J. Vuckovic, A. Scherer, Defect modes of a two-dimensional photonic crystal in an optically thin dielectric slab, J. Opt. Soc. Am. B 16 (1999) 275–285.
[34] H. Benisty, et al., Radiation losses of waveguide-based two-dimensional photonic crystals: Positive role of the substrate, Appl. Phys. Lett. 76 (2000) 532–534.
[35] A. Chutinan, S. Noda, Waveguides and waveguide bends in two-dimensional photonic crystal slabs, Phys.Review B 62 (2000) 4488–4492.
[36] S. Kuchinsky, D.C. Allan, N.F. Borrelli, J.-C. Cotteverte, 3D localization in a channel waveguide in a photonic crystal with 2D periodicity, Opt. Commun. 175 (2000) 147–152.
[37] S.Y. Lin, E. Chow, S.G. Johnson, J.D. Joannopoulos, Demonstration of highly efficient waveguiding in a photonic crystal slab at the 1.5-um wavelength, Opt. Lett. 25 (2000) 1297–1299.
[38] V. Pacradouni, et al., Photonic band structure of dielectric membranes periodically textured in two dimensions, Phys. Rev. B 62 (2000) 4204–4207.
[39] B. Cunningham, P. Li, B. Lin, J. Pepper, Colorimetric resonant reflection as a direct biochemical assay technique, Sens. Actuat. B-Chem. 81 (2002) 316–328. http://dx.doi.org/10.1016/S0925-4005(01)00976-5.
[40] B. Cunningham, et al., A plastic colorimetric resonant optical biosensor for multiparallel detection of label-free biochemical interactions, Sens. Actuat. B-Chem. 85 (219-226) (2002) doi:Pii S0925-4005(02)00111-9.
[41] B.T. Cunningham, et al., Label-free assays on the BIND system, J Biomol Screen 9 (2004) 481–490. http://dx.doi.org/10.1177/1087057104267604.
[42] W. Chen, et al., Photonic crystal enhanced microscopy for imaging of live cell adhesion, Analyst 138 (2013) 5886–5894. http://dx.doi.org/10.1039/c3an01541f.
[43] Y. Zhuo, et al., Single nanoparticle detection using photonic crystal enhanced microscopy, Analyst 139 (2014) 1007–1015. http://dx.doi.org/10.1039/C3an02295a.
[44] J.N. Liu, M.V. Schulmerich, R. Bhargava, B.T. Cunningham, Sculpting narrowband Fano resonances inherent in the large-area mid-infrared photonic crystal microresonators for spectroscopic imaging, Opt. Express 22 (2014) 18142–18158. http://dx.doi.org/10.1364/OE.22.018142.
[45] P. Yeh, A. Yariv, A.Y. Cho, Optical surface waves in periodic layered media, Appl. Phys. Lett. 32 (1978) 104–105.
[46] R. Barer, Interference microscopy and mass determination, Nature 169 (1952) 366–367.
[47] R. Barer, Determination of dry mass, thickness, solid and water concentration in living cells, Nature 172 (1953) 1097–1098.
[48] R. Barer, K.F. Ross, S. Tkaczyk, Refractometry of living cells, Nature 171 (1953) 720–724.
[49] R.J. Vasquez, B. Howell, A.-M.C. Yvon, P. Wadsworth, L. Cassimeris, Nanornolar Concentrations of Nocodazole Alter Microtubule Dynamic Instability In Vivo and In Vitro, Mol. Biol. Cell 8 (1997) 973–985.
[50] M. Machacek, et al., Coordination of Rho GTPase activities during cell protrusion, Nature 461 (2009) 99–103. http://dx.doi.org/10.1038/nature08242.
[51] K. Otsu, R. Kishigami, N. Fujiwara, K. Ishizeki, H. Harada, Functional role of Rho-kinase in ameloblast differentiation, J. C ell. Physiol. 226 (2011) 2527–2534. http://dx.doi.org/10.1002/jcp.22597.
[52] M. Valtieri, et al., Cytokine-dependent granulocytic differentiation. Regulation of proliferative and differentiative responses in a murine progenitor cell line, J. Immunol. 138 (1987) 3829–3835.
[53] A. Aglianó, et al., On chromosomal instability: what is the karyotype of your 32D CI3 cell line, Blood 95 (2000) 3636–3637.
[54] J. Banks, L. Mozdzen, B. Harley, R. Bailey, The combined effects of matrix stiffness and growth factor immobilization on the bioactivity and differentiation capabilities of adipose-derived stem cells, Biomaterials 35 (2014) 8951–8959.
[55] E. Monaco, et al., Morphological and transcriptomic comparison of adipose and bone marrow derived porcine stem cells, Open Tissue Eng. Regen. Med. J. 2 (2009) 20–33.
[56] S. Pedron, E. Becka, B. Harley, Spatially-gradated hydrogel platform as a three-dimensional engineered tumor microenvironment, Adv. Mater. 27 (2015) 1567–1572.
[57] Y. Zhuo, B.T. Cunningham, Label-free biosensor imaging on photonic crystal surfaces, Sensors (Basel) 15 (2015) 21613–21635. http://dx.doi.org/10.3390/s150921613.
[58] M. Mir, B. Bhaduri, R. Wang, R. Zhu, G. Popescu, in: Progress in Optics, Elsevier, Vol. 57, 2012, pp. 133–217.